Monthly Notices of the ROYAL ASTRONOMICAL SOCIETY

MNRAS **535,** 2670–2686 (2024) https://doi.org/10.1093/mnras/stae2504
Advance Access publication 2024 November 6

Systematic opacity calculations for kilonovae – II. Improved atomic data for singly ionized lanthanides

Daiji Kato [1,2]★ Masaomi Tanaka [3,4]★ Gediminas Gaigalas [5] Laima Kitovienė[5] and Pavel Rynkun [5]

[1]*National Institute for Fusion Science, 322-6 Oroshi-cho, Toki 509-5292, Japan*
[2]*Interdisciplinary Graduate School of Engineering Sciences, Kyushu University, Kasuga, Fukuoka 816-8580, Japan*
[3]*Astronomical Institute, Tohoku University, Sendai 980-8578, Japan*
[4]*Division for the Establishment of Frontier Sciences, Organization for Advanced Studies, Tohoku University, Sendai 980-8577, Japan*
[5]*Institute of Theoretical Physics and Astronomy, Vilnius University, Saulėtekio Ave 3, LT-10257 Vilnius, Lithuania*

Accepted 2024 October 31. in original form 2024 September 17

ABSTRACT

Lanthanides play the most important roles in the opacities for kilonova, ultraviolet–optical–infrared emission from neutron star mergers. Although several efforts have been made to construct atomic data, the accuracy of the opacity is not fully assessed and understood. In this paper, we perform atomic calculations for singly ionized lanthanides with improved strategies, aiming at understanding the physics of the lanthanide opacities in kilonova ejecta and necessary accuracy in atomic data. Our results show systematically lower energy level distributions as compared with our previous study (Paper I). As a result, the opacities evaluated with our new results are higher by a factor of up to 3–10, depending on the element and wavelength range. For a lanthanide-rich element mixture, our results give a higher opacity than that in Paper I by a factor of about 1.5. We also present opacities by using the results of *ab initio* atomic calculations by using GRASP2K code. In general, our new opacities show good agreements with those with *ab initio* calculations. We identify that structure of the lanthanide opacities is controlled by transition arrays among several configurations, for which derivation of accurate energy level distribution is important to obtain reliable opacities.

Key words: atomic data – opacity – neutron star mergers.

1 INTRODUCTION

Neutron star (NS) mergers have been expected to be a promising site for a rapid neutron capture process (r-process; e.g. Lattimer & Schramm 1974; Eichler et al. 1989; Goriely, Bauswein & Janka 2011; Korobkin et al. 2012; Bauswein, Goriely & Janka 2013; Wanajo et al. 2014). The ejected material (or ejecta) can emit thermal electromagnetic radiation, so-called kilonova, which is powered by radioactive decays of newly synthesized r-process nuclei (e.g. Li & Paczyński 1998; Metzger et al. 2010). By reflecting the temperature and opacities in the ejecta, kilonova emission is expected to be mainly in ultraviolet (UV), optical, and infrared (IR) wavelengths for a time-scale of about 1–10 d after the merger (e.g. Metzger et al. 2010; Barnes & Kasen 2013; Kasen, Badnell & Barnes 2013; Tanaka & Hotokezaka 2013; Metzger & Fernández 2014).

In 2017, by following the detection of gravitational waves from a NS merger (GW170817; Abbott et al. 2017a), an electromagnetic counterpart has been observed (Abbott et al. 2017b). In UV, optical, and IR wavelengths, the counterpart (AT2017gfo) shows thermal emission. The properties of AT2017gfo are broadly consistent with expected properties of kilonova (e.g. Kasen et al. 2017; Perego, Radice & Bernuzzi 2017; Tanaka et al. 2017; Kawaguchi, Shibata & Tanaka 2018; Rosswog et al. 2018), confirming r-process nucleosynthesis in NS merger.

Properties of kilonova, i.e. luminosity, time-scale, and colour or spectral shapes, are mainly determined by the mass and velocity of the ejecta and elemental compositions in the ejecta. In particular, elemental compositions play important roles as they control the opacity in the ejecta. In the NS merger ejecta, with a typical temperature of $T \sim 10^3$–10^5 K, the main opacity source is the bound–bound transitions of heavy elements. In particular, lanthanides (atomic number $Z = 57$–71) have high opacities by reflecting their dense energy levels (Kasen et al. 2013; Tanaka & Hotokezaka 2013; Fontes et al. 2020; Tanaka et al. 2020). Thus, the presence or absence of lanthanides largely affects the light curves of kilonova. Thanks to these properties, we can infer the nucleosynthesis in NS mergers through observational data of kilonovae.

To reliably connect the nucleosynthesis information with observed properties of kilonovae, accurate understanding of the opacities in NS merger ejecta is crucial. The opacities are determined by a large number of transitions including those from excited states. Thus, complete energy levels and transition probabilities are necessary to evaluate the opacity, even under the simplest assumption of local thermodynamic equilibrium (LTE). Since it is not yet practical to derive such complete information from experimental data, current understanding of the kilonova opacities relies on theoretical atomic

★ E-mail: kato.daiji@nifs.ac.jp (DK); masaomi.tanaka@astr.tohoku.ac.jp (MT)

Table 1. Strategy for effective potentials. The second column shows occupied orbitals of equation (1). Inner shells: n = 1–3, 4spd, and 5sp are fully occupied. The potentials for orbitals with (g) were weighted average as in equation (3). The third column shows electronic configurations included in the first-order energy minimization. $\Delta_{\rm median}$ is the median of absolute values of deviation from the reference values, i.e. $\Delta = |E - E^{(\rm ref)}|/E^{(\rm ref)}$, in per cent for the calculated lowest levels (see text for more details). Note that the strategy of Yb II is the same as in Paper I.

Ion	Potential	First-order energy	$\Delta_{\rm median}$
Pr II	$4f^3$	$4f^3$ 6s	12
Nd II	$4f^4$	$4f^4$ 6s	25
Pm II	$4f^4$ 6s (g)	$4f^5$ 6s	17
Sm II	$4f^5$ 5d	$4f^6$ 6s	13
Eu II	$4f^7$	$4f^7$ 6s	13
Gd II	$4f^7$ 5d	$4f^8$ 6s	42
Tb II	$4f^8$ 5d	$4f^9$ 6s	23
Dy II	$4f^{10}$	$4f^{10}$ 6s	16
Ho II	$4f^{10}$ 5d	$4f^{11}$ 6s	18
Er II	$4f^{11}$ 5d	$4f^{12}$ (6s, 5d, 6p), $4f^{11}$ $6s^2$	11
Tm II	$4f^{12}$ 6s	$4f^{13}$ 6s	14
Yb II	$4f^{14}$ (g)	$4f^{14}$ (6s, 5d, 6p, 7s), $4f^{13}$ $6s^2$	14

calculations. In fact, there has been significant progress in the atomic calculations for application to kilonovae in the past decade (e.g. Kasen et al. 2017; Tanaka et al. 2018, 2020; Wollaeger et al. 2018; Gaigalas et al. 2019; Banerjee et al. 2020, 2024; Fontes et al. 2020, 2023; Carvajal Gallego et al. 2023, 2024b). Thanks to these efforts, atomic opacities for essentially all the elements relevant to kilonova have been constructed (up to about 10th ionization).

However, the accuracy of the opacities is not entirely assessed. Due to the complexity, theoretical atomic calculations covering many elements and ionization stages often involve simplifications in the calculations, such as a parametrized effective potential. Some studies have studied the accuracy of the results, but such works only focused on one or a few elements (Tanaka et al. 2018; Gaigalas et al. 2019; Flörs et al. 2023). It is, thus, not yet clear in general how good the accuracy of the currently available opacities is. In particular, since lanthanides give the dominant opacities in kilonovae, it is important to understand which configurations play important roles to the lanthanide opacities and how good accuracy is necessary to derive the reliable opacities.

Recently, we have performed *ab initio* calculations for singly ionized lanthanides covering 12 elements with Z = 59–70 (Gaigalas et al. 2019, hereafter G19; Radžiūtė et al. 2020, hereafter R20; Radžiūtė et al. 2021, hereafter R21) by using GRASP2K code (Jönsson et al. 2013). The calculated energy levels and transition probabilities are intensively compared with available atomic data, and thus, the atomic data serve as benchmark results for singly ionized lanthanides. Due to the computational cost, it is not practical to perform such detailed calculations covering all the elements and ionization states which are important in kilonova. Thus, it is also important to provide accurate atomic data with more approximated calculations, which can cover many elements and ionization states as demonstrated in our previous work (Tanaka et al. 2020, hereafter Paper I).

In this paper, by using the privilege of G19, R20, and R21, we aim to obtain a deeper understanding of the lanthanide opacities in kilonova ejecta, and at finding a pathway to provide accurate atomic data with approximated calculations. In Section 2, we perform atomic calculations using HULLAC code (Bar-Shalom, Klapisch & Oreg 2001) with improved strategies as compared with those in Paper I. In Section 3, we calculate the opacities using our new results and results from G19, R20, and R21. In Section 4, we discuss properties of lanthanide opacities and implication to kilonova. Finally, we summarize the paper in Section 5.

2 ATOMIC CALCULATIONS

2.1 HULLAC calculations

In HULLAC, the relativistic configuration interaction (RCI) method is performed using solutions of the single-electron Dirac equation with an effective central-field potential. The accuracy of the RCI calculations is improved basically by increasing the number of configurations. However, the size of the configurations can be exceedingly large for lanthanide due to the existence of an open 4f shell. To reduce computational costs, we restricted the RCI to the minimal set of configurations of low energies that are most relevant to transitions of the opacity, i.e. $4f^q$ (6s, 5d, 6p) and $4f^{q-1}\left(5d^2, 5d\,6s, 6s^2, 6s\,6p, 5d\,6p\right)$, q = 3–14 for each element, respectively (more details will be discussed in Section 4). For Sm II and Yb II, $4f^7$ and $4f^{14}$ 7s were also added, respectively. In the present calculations, therefore, we can improve the accuracy of the results by optimizing the effective potential.

In HULLAC, the effective potential for N-electron ions of the nuclear charge Z is expressed as

$$U(r) = -\frac{1}{r}\left[(Z - N + 1) + \sum_i q_i\, f_{l_i,\alpha_i}(r)\right], \tag{1}$$

where q_i is occupation numbers for the orbitals $(nl)_i$, and the total occupation number, $\sum q_i = N - 1$. $f_{l,\alpha}(r)$ is obtained from the Slater-type charge distribution of an electron of the azimuthal quantum number l, which is expressed as

$$f_{l,\alpha}(r) = \mathrm{e}^{-\alpha r}\sum_{k=0}^{2l+1}\left(1 - \frac{k}{2l+2}\right)\frac{(\alpha r)^k}{k!}, \tag{2}$$

where α is related to the mean radius of the charge distribution by $\alpha = (2l+3)/\langle r\rangle$. For closed shells, the weighted average of $f_{l,\alpha}(r)$ is used,

$$g_{L,\alpha}(r) = \frac{1}{2(L+1)^2}\sum_{l=0}^{L}(4l+2)\,f_{l,\alpha^{(l)}}(r), \tag{3}$$

where $L \le n - 1$, and α and $\alpha^{(l)}$ in the average are dependent on

$$\alpha^{(l)} = \alpha \times \frac{l+1}{1-\eta(l+1)}, \quad \eta = 0.05. \tag{4}$$

Note that the potential of equation (1) satisfies the correct asymptotic conditions,

$$\lim_{r\to 0} U(r) = -\frac{Z}{r}, \lim_{r\to\infty} U(r) = -\frac{Z-N+1}{r}. \tag{5}$$

With a given set of the occupation numbers q_i, values of the α_i were varied until the expectation value of the energy (the first-order energy) for the ground state and low-lying excited states became minimum by the Nelder–Mead method. The energy minimization was performed for several sets of the occupation numbers for the potential.

Then, we compared the calculated lowest energy level for each configuration with the value in the NIST Atomic Spectral Database (ASD; Kramida et al. 2018). For Pm II and Ho II, however, we compared also with the GRASP results (R20 for Pm II and R21 for Ho II) for higher excited states since the data available in the data base are limited. The agreement was evaluated by the

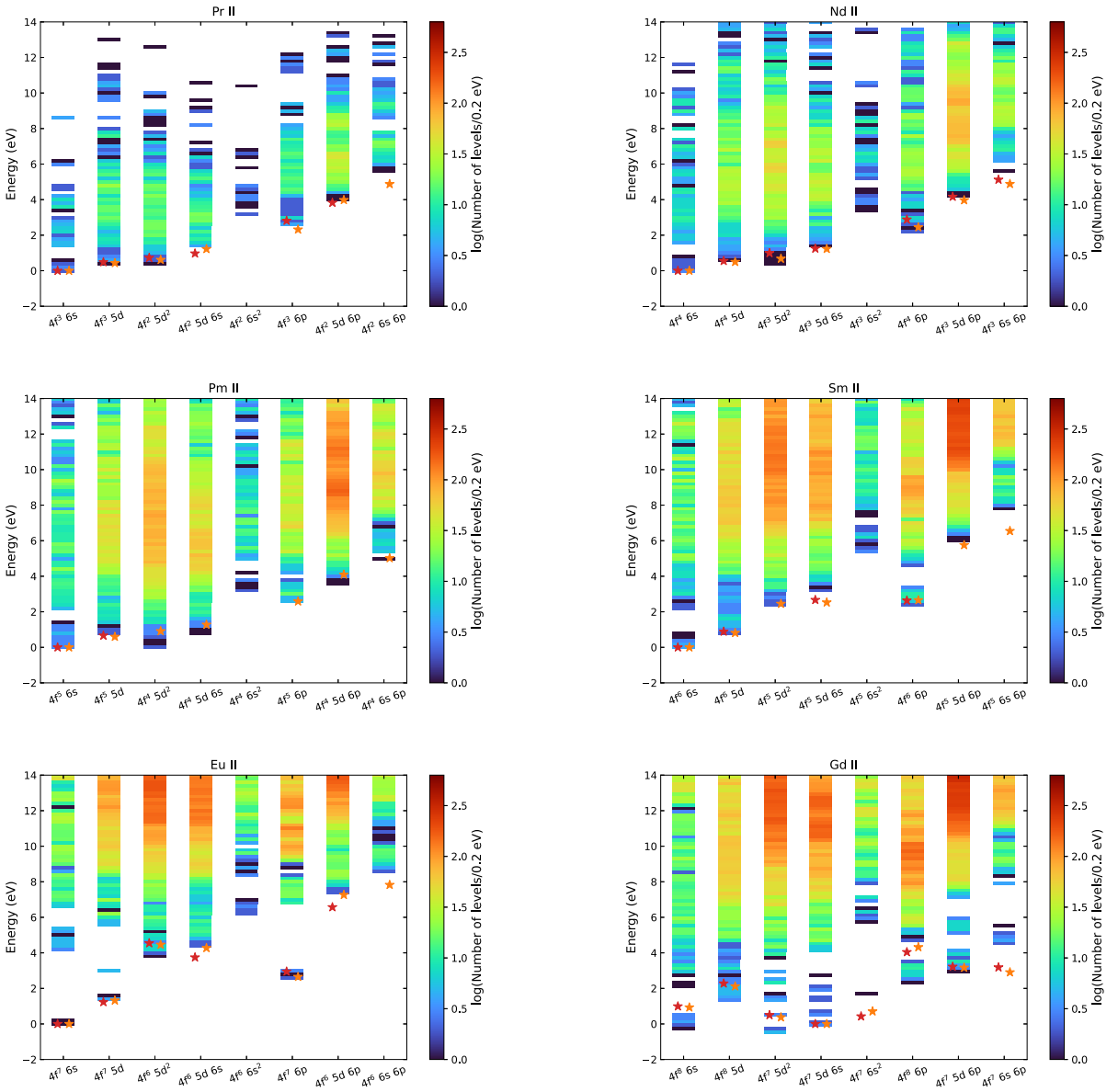

Figure 1. Calculated energy levels distribution for singly ionized ions ($Z = 59$–64). The energy levels are shown for each configuration. The colours represent the number of energy level in 0.2 eV bin. The red (on the left side) and orange (on the right side) star symbols represent the lowest energy for each configuration from the NIST ASD and GRASP calculations (G19; R20; R21), respectively. The energy is measured from the lowest level of the correct ground state in the NIST ASD, i.e. $4f^7$ 5d 6s for Gd II and $4f^q$ 6s for the others. Energy levels above $E = 14$ eV are also calculated, but they are not shown in this figure to highlight the lower energy levels.

median of absolute values of normalized errors from the reference values, i.e. $\Delta = |E - E^{(\mathrm{ref})}|/E^{(\mathrm{ref})}$, accounting for the lowest levels of $4f^q$ (6s, 5d, 6p) and $4f^{q-1}$ $\left(5d^2, 5d\,6s, 6s^2, 6s\,6p, 5d\,6p\right)$, where E is measured from the lowest level of the correct ground state in the NIST ASD. The best strategies for the potentials in the present calculations are summarized in Table 1.

2.2 Results

Figs 1 and 2 show the calculated energy level distributions for each configuration and element. In the figures, the lowest levels of each configuration from the NIST ASD and GRASP results (G19 for Nd, R20 for Pr and Pm–Gd, and R21 for Tb–Yb, respectively) are also plotted for comparison (marked by stars). The differences are 10–25 per cent in the median, except for Gd II (42 per cent; see Table 1). This agreement is significant as compared with Paper I that remained much larger differences (20–100 per cent).

We optimized the potential for Gd II to the excited state $4f^8$ 6s exceptionally because the potential optimized to the ground state as for the other elements, i.e. $4f^7$ 5d 6s for Gd II, gave the lowest levels of $4f^8$ nl configurations far high from reference values of the NIST ASD. As a result, the low-lying levels of $4f^7$ $5d^2$ and $4f^8$ 6s spread below the lowest level of $4f^7$ 5d 6s in the present calculations. Nevertheless, the median of the errors from the reference values is

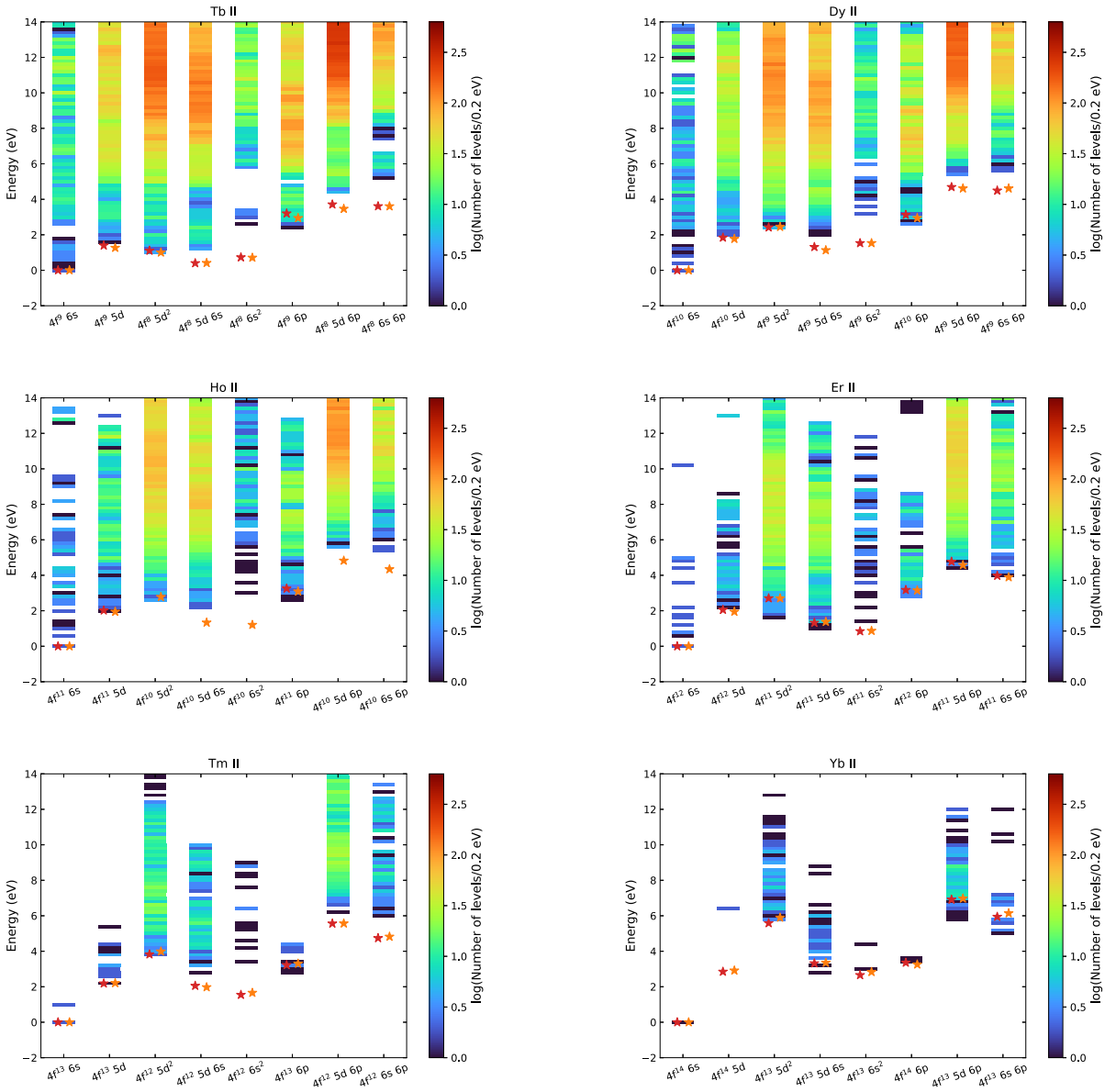

Figure 2. Same with Fig. 1, but for the elements with $Z = 65$–70.

smaller than that obtained with the potential optimized to the correct ground state.

It may be noteworthy that the energy sequence of the $4f^{q-1}(5d^2, 5d\ 6s, 6s^2)$ levels seems different for light and heavy lanthanides: the energy levels of the $5d^2$ become higher for heavy lanthanides, while those of the $6s^2$ become relatively lower. This can be ascribed to variation of the binding energies of the 5d and 6s orbitals along Z. As Z increases, the 5d orbital becomes more loosely bounded due to screening of the nuclear charge, while the 6s orbital has an almost constant binding energy for $Z = 59$–69. Therefore, because substituting electrons from the inner 4f orbital to the 5d orbital becomes energetically more unfavourable, the $5d^2$ levels become higher, and the $6s^2$ levels become relatively lower for heavy lanthanides.

The present calculations give basically lower level distributions of excited states than those of Paper I. Fig. 3 shows examples for Sm II and Ho II below 6 eV. It is clear that the present calculations of cumulative level distributions tend to be consistent with the GRASP results. The lowering of the excited states level distributions will in principle give more bound–bound transitions at longer wavelengths resulting in an increase of the opacity (see Section 3). A comparison of the number of levels in 6 eV from the ground level is given for all the elements of $Z = 59$–70 in Table 2. The table also shows the total number of levels obtained by the present RCI calculations for each configuration. Assignment of the configuration is done by the leading composition of the eigenvector.

3 OPACITY CALCULATIONS

3.1 Methods

By using the results of atomic calculations described in Section 2, we calculate the bound–bound opacities in the ejecta of NS merger.

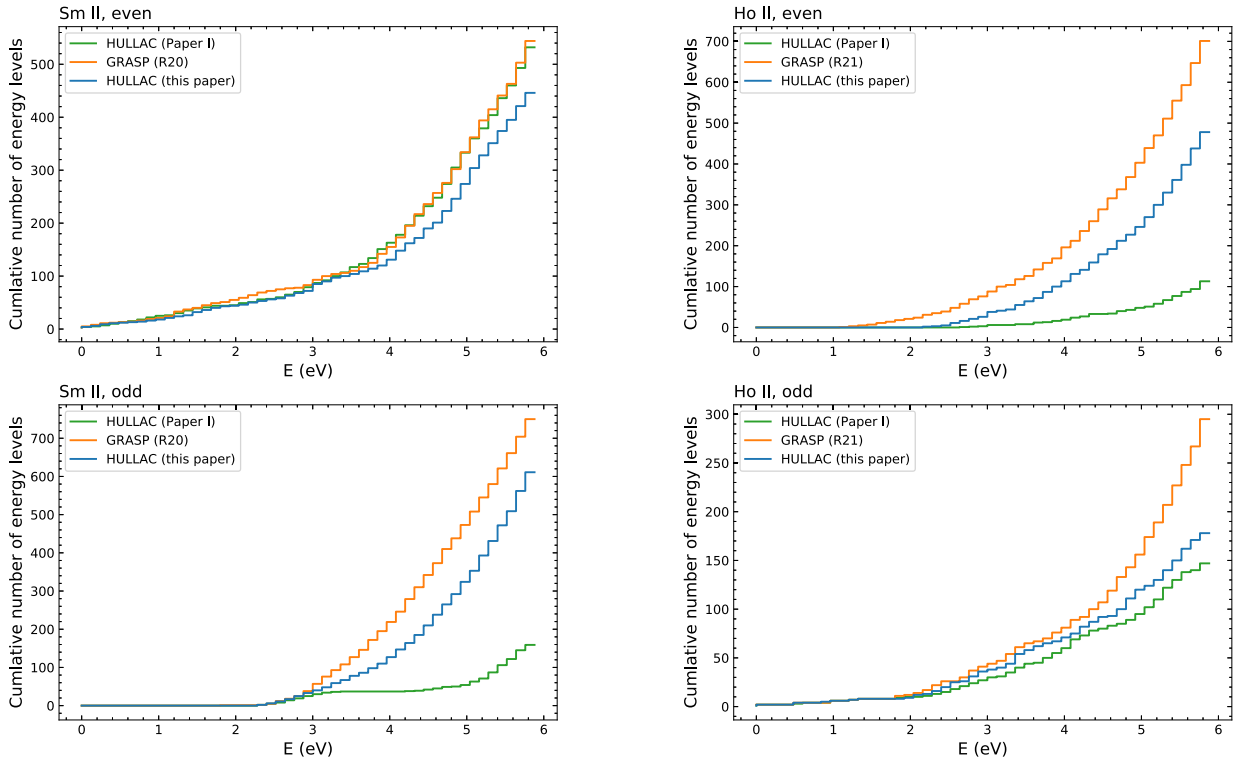

Figure 3. Cumulative number distributions of the energy levels of Sm II and Ho II for each parity.

As we follow the same methods as in Paper I, here we only give a brief overview. In the rapidly expanding medium with a large velocity gradient, such as ejecta of supernova or NS merger, the bound–bound opacity for a certain wavelength grid ($\Delta\lambda$) can be evaluated by so-called expansion opacity formalism (e.g. Karp et al. 1977; Eastman & Pinto 1993; Kasen, Thomas & Nugent 2006):

$$\kappa_{\rm exp}(\lambda) = \frac{1}{ct\rho}\sum_l \frac{\lambda_l}{\Delta\lambda}\left(1-{\rm e}^{-\tau_l}\right). \quad (6)$$

Here λ_l and τ_l are the transition wavelength and the Sobolev optical depth for each transition, respectively, ρ is mass density, and t is time after the merger. The summation in the equation is taken over all the bound–bound transitions in a certain wavelength bin. In the case of homologous expansion ($r = vt$), which is a sound assumption in the ejecta at the epoch of interest ($t >$ a few hours), the Sobolev optical depth is expressed as

$$\tau_l = \frac{\pi e^2}{m_{\rm e}c} f_l n_{i,j,k} t \lambda_l, \quad (7)$$

where f_l is the oscillator strength of the transition and $n_{i,j,k}$ is the number density of ith element in jth ionization state and kth excited state.

We calculate ionization and excitation under the assumption of LTE. By Boltzman distribution, $n_{i,j,k} = n_{i,j}(g_k/\Sigma_{i,j}(T))\exp(-E_k/kT)$, where g_k and E_k are a statistical weight and energy of the lower level of the transition, respectively. Here $\Sigma_{i,j}(T)$ is the partition function for the ith element at jth ionization state.[1] The number density of the ion $n_{i,j}$ is evaluated by solving the Saha equation. To derive the ionization degrees, we also need the partition functions for ionization states other than singly ionized states. For these, we used the results of Paper I.

3.2 Results

In Figs 4 and 5, we show the expansion opacity at $t = 1$ d as a function of wavelength for each element. The opacities are calculated for $\rho = 10^{-13}$ g cm^{-3} and $T = 5000$ K, which is a typical plasma condition for the NS merger ejecta with an ejecta mass of an order of 0.01 $M_\odot$ and a typical velocity of about $v \sim 0.1c$ at $t = 1$ d. We choose this early time ($t = 1$ d) as deviation from LTE is known to be significant in particular in the outer ejecta after several days after the merger (Hotokezaka et al. 2021; Pognan, Jerkstrand & Grumer 2022).

In Figs 4 and 5, it is assumed that the ejecta consists of single element (see Section 4 for more realistic elemental compositions). To compare the opacity calculated from different atomic data, we calculate the opacity only for the singly ionized states as GRASP data are available only for the singly ionized state. Note that we still solve the ionization to derive the number density of each ion $n_{i,j}$. At the adopted density and temperature, singly ionized states give dominant contributions to the opacities.

As shown in Figs 4 and 5, the opacities evaluated with our new atomic data are generally higher than those in Paper I. In

[1] In our previous works to calculate the opacities (Tanaka & Hotokezaka 2013; Tanaka et al. 2018), we assumed $n_{i,j,k} = n_{i,j}(g_k/g_0)\exp(-E_k/kT)$, and g_0 is evaluated as a sum of the statistical weight for the levels with the same LS term with the ground level as there were no atomic data covering the entire energy spectra are available. In Paper I, we also used the same scheme. In this paper (and also Banerjee et al. 2024), we calculate a temperature-dependent partition function. We confirmed that the previous assumption has a negligible impact on the opacity in the temperature range of interest ($T < 25\,000$ K).

Table 2. Comparison of the number of levels for each parity in 6 eV from the ground level. The first and second rows are HULLAC results of the present calculation and Paper I, respectively, and the third row is GRASP results from G19 for Nd, R20 for Pr and Pm–Gd, and R21 for Tb–Yb, respectively. For Yb II, the present results and those of Paper I are identical as the same strategy was used. The total number of levels by the present RCI calculation is also shown for each configuration in the following columns.

Ion	$N_{\rm level}$ ($\leq$6 eV)		$4f^q$ 6s	$4f^q$ 5d	$4f^{q-1}$ 5d^2	$4f^{q-1}$ 5d 6s	$4f^{q-1}$ 6s^2	$4f^q$ 6p	$4f^{q-1}$ 5d 6p	$4f^{q-1}$ 6s 6p
	Even	Odd								
Pr II ($q=3$)	700	523	87	358	392	242	22	270	601	186
	679	486								
	758	731								
Nd II ($q=4$)	690	1213	256	896	1438	801	113	687	2048	690
	647	970								
	929	1337								
Pm II ($q=5$)	1874	895	598	1793	3575	2072	340	1465	5165	1694
	576	792								
	1466	1113								
Sm II ($q=6$)	446	611	1002	2949	6141	4225	517	2521	9456	3133
	532	159								
	544	750								
Eu II ($q=7$)	140	50	1387	4231	8977	6051	936	3544	13 513	4109
	103	48								
	137	85								
Gd II ($q=8$)	301	327	1256	3537	9169	6882	1204	4238	15 298	5149
	68	235								
	270	222								
Tb II ($q=9$)	820	538	841	3042	8552	5987	942	3267	13 437	4434
	862	352								
	925	851								
Dy II ($q=10$)	273	698	370	1667	5986	4345	555	1658	9182	3205
	231	535								
	458	951								
Ho II ($q=11$)	478	178	108	559	3351	2279	251	645	2279	1814
	113	147								
	701	295								
Er II ($q=12$)	162	628	25	123	1411	852	75	159	2028	660
	151	448								
	188	534								
Tm II ($q=13$)	188	24	4	20	453	213	17	13	602	162
	223	34								
	238	44								
Yb II ($q=14$)	3	27	1	2	81	39	2	2	113	24
	3	27								
	3	42								

particular, the opacities of Pm II, Sm II, Eu II, Gd II, Tb II, Dy II, Ho II, and Er II at <5000 Å show a large deviation up to by a factor of about 10. These differences stem from the energy distribution as discussed in Section 2. Our improved calculations tend to show lower energy level distributions as compared with Paper I. As a result, the number of strong transitions increases with the higher population of excited states through the Boltzmann factor $\exp(-E_l/kT)$.

Our new opacities show reasonable agreements with those calculated with the results of GRASP calculations (G19; R20; R21). In particular, for the elements with a large opacity increase with respect to Paper I, the agreement between our new opacities and GRASP opacities is quite well in particular at <5000 Å. However, there are still a few cases that show a large discrepancy at 5000–10 000 Å (Tb II, Dy II, and Ho II). This is discussed in Section 4 in more detail.

Fig. 6 summarizes our results for all the elements with $Z = 59$–70. To define a characteristic opacity for each element, we evaluate Planck mean opacity with $T = 5000$ K. As discussed above, the newly calculated opacities are in general higher than those in Paper I, giving a better agreement with GRASP opacities. The entire temperature dependences of the Planck mean opacities are shown in Appendix A (Figs A1 and A2).

4 DISCUSSIONS

4.1 Properties of lanthanide opacities

We have performed atomic calculations for singly ionized lanthanides with HULLAC code with improved strategies. We show that, compared with our previous calculations in Paper I, the overall energy level distributions are shifted toward lower energy. This results in an increase of the opacities through the higher populations of excited levels for a given temperature.

To understand which configurations play important roles in the lanthanide opacities, we here analyse the calculated opacities. As demonstrated in G19, the number of strong lines as a function of

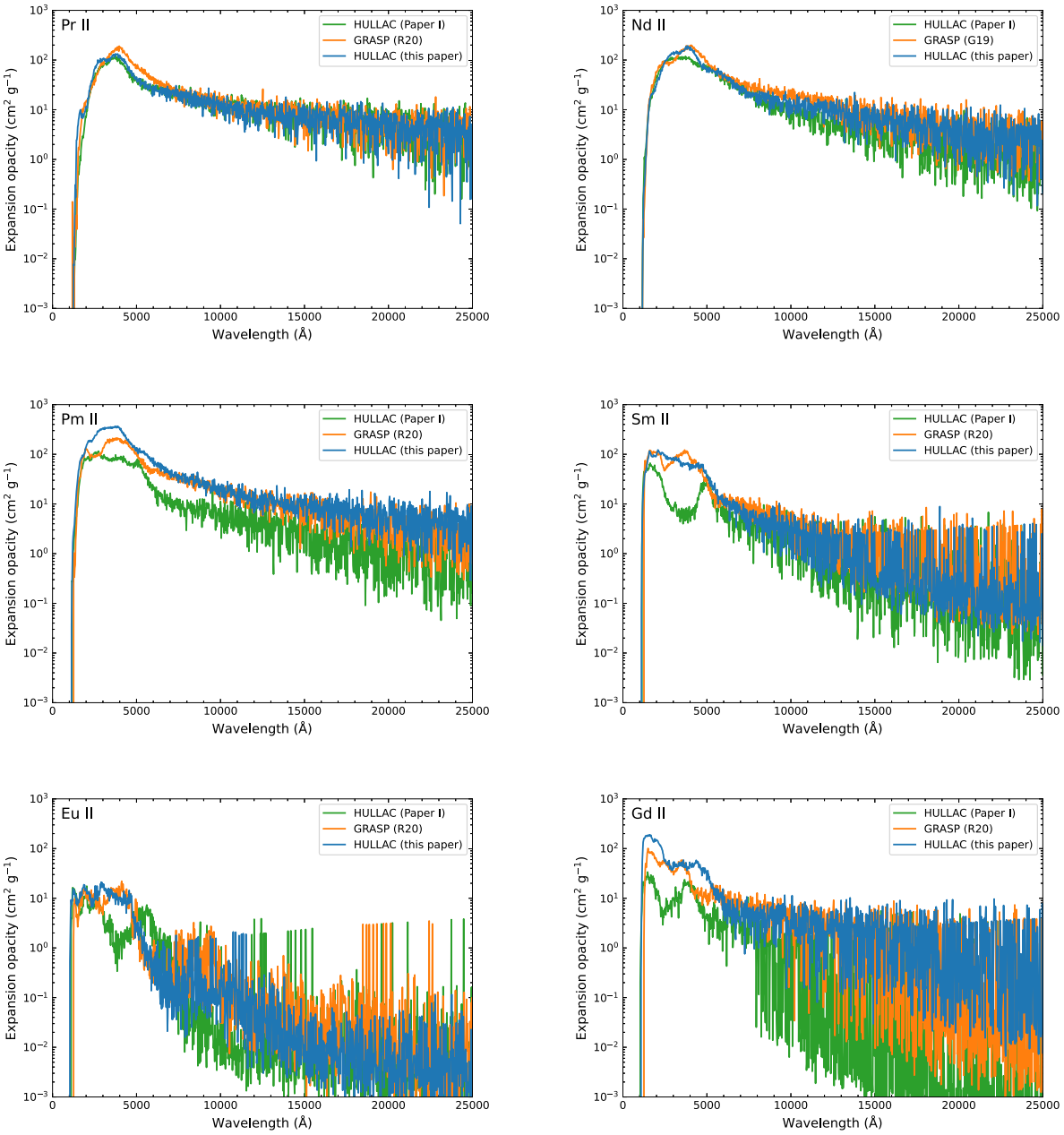

Figure 4. Expansion opacity as a function of wavelength for singly ionized lanthanides ($Z = 59$–64). The opacities are those for $\rho = 10^{-13}$ g cm^{-3} and $T = 5000$ K at $t = 1$ d after the merger.

wavelength gives a good measure of the opacity as the expansion opacity is determined by the sum of $1 - \exp(-\tau_l)$ for each wavelength bin. Here, by following G19, we select strong lines that satisfy $gf \exp(-E_l/kT) > 10^{-5}$ at $T = 5000$ K. Table 3 summarizes the number of strong lines satisfying the condition above for each ion.

The results of the analysis are shown for the case of Sm II in Fig. 7. The black lines show the number of strong lines for Sm II as a function of wavelength. The left panels show that break down of the number of lines according to the lower level configurations, while the right panels show the same according to the upper level configurations. The same analysis is shown for our HULLAC calculations in Paper I (top), GRASP calculations from R20 (middle), and our new HULLAC calculations in this paper (bottom). It is confirmed that the black line in each calculation represents the characteristic features in the opacity, as demonstrated by G19 for Nd.

At $\lambda < 6000$ Å, the strong lines are dominated by those from $4f^6$ 6s as a lower configuration, followed by those from $4f^6$ 5d, $4f^6$ 6p, $4f^5$ 5d 6s, and $4f^5$ $5d^2$. The corresponding upper configurations for these strong lines are either $4f^5$ $5d^2$, $4f^5$ 5d 6s, $4f^6$ 6p, or $4f^5$ 5d 6p. At $\lambda > 6000$ Å, the lower configuration of strong lines is almost entirely $4f^6$ 5d. The corresponding upper configurations are either $4f^6$ 6p or $4f^5$ $5d^2$.

From this analysis, we can understand the reason why the opacity of Sm II in Paper I is smaller than that from GRASP calculations (R20) and our HULLAC calculations in this paper. In Paper I, atomic calculations for Sm II did not include $4f^5$ $5d^2$ and $4f^5$ 5d 6p config-

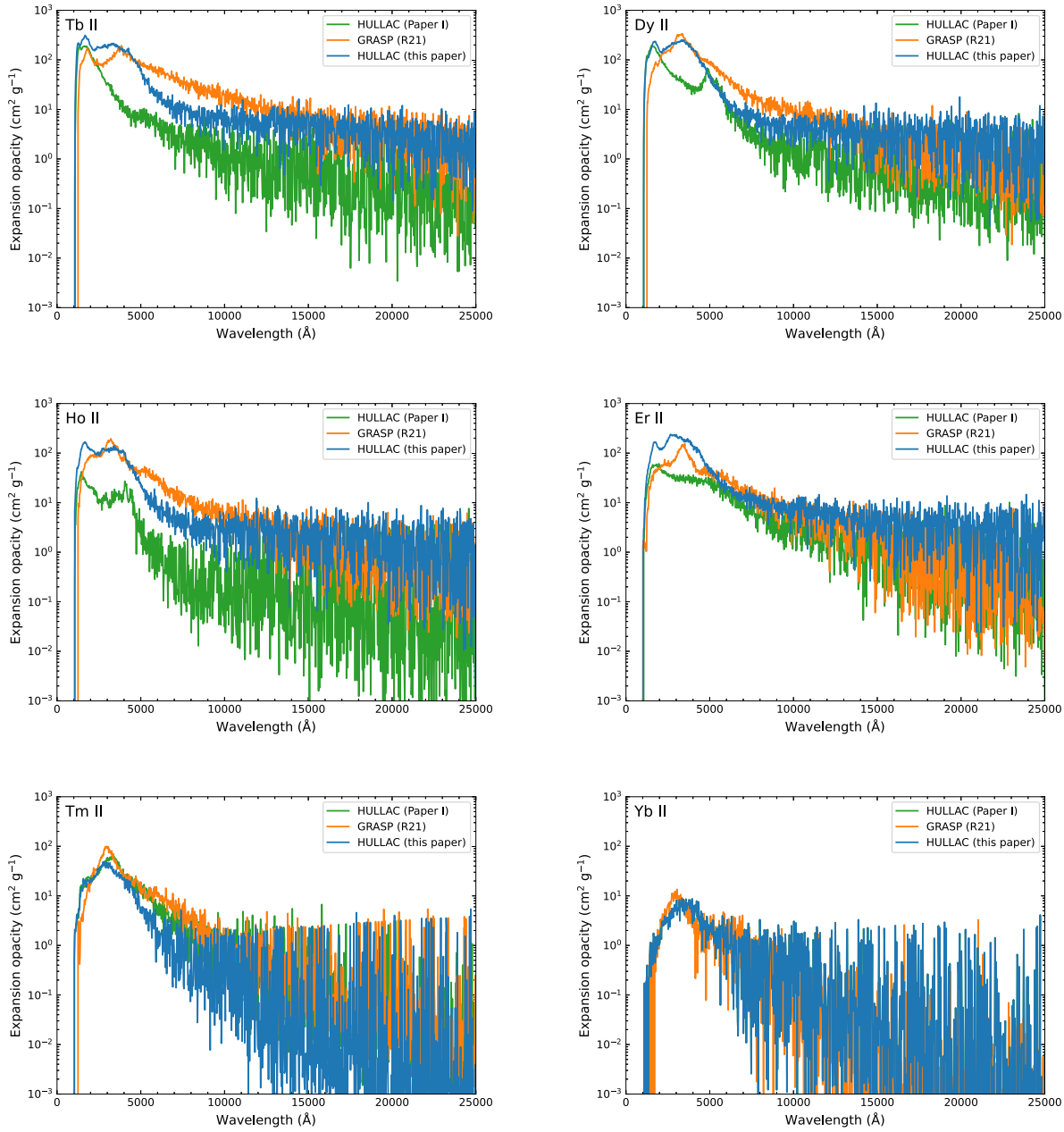

Figure 5. Same as Fig. 4, but for $Z = 65$–70. Note that the HULLAC results for Yb II in Paper I and this paper are identical.

urations. As shown in the GRASP calculations (R20) and the HULLAC calculations in this paper, $4f^5\ 5d^2$ configuration is important as a lower configuration, and both $4f^5\ 5d^2$ and $4f^5\ 5d\ 6p$ configurations are important as upper configurations. Thus, the lack of these two configurations causes a strong dip in the opacity around 3000–4000 Å.

Overall, a similar trend can be seen in the case of Ho II as shown in Fig. 8. In this case, the low opacity in Paper I is caused by lack of $4f^{10}\ 5d^2$ as upper configurations and upward energy distribution of $4f^{10}\ 5d\ 6s$ configuration. For Ho II, our HULLAC calculations and GRASP calculations (R21) still give a relatively large discrepancy in the opacities at $\lambda > 5000$–10 000 Å. This is due to the higher energy levels of $4f^{10}\ 5d^2$ configuration in the HULLAC calculations (see even parity in Fig. 3).

It is interesting that transitions between the levels of certain configurations are clustered in wavelength, forming 'transition array', as also discussed in Carvajal Gallego et al. (2024a). Since lanthanides have a large number of excited levels with small energy separation, many transitions can be clustered in a similar wavelength range. The transition arrays for singly ionized lanthanides are summarized in Fig. 9. Our results demonstrate that it is important (i) to include these configurations in the atomic structure calculations to secure the completeness of the transitions, and (ii) to derive the accurate energy levels for these configurations to obtain reliable opacities.

4.2 Opacities of element mixture

So far we have shown opacities for each element. In realistic kilonova ejecta, however, a variety of elements coexist in the

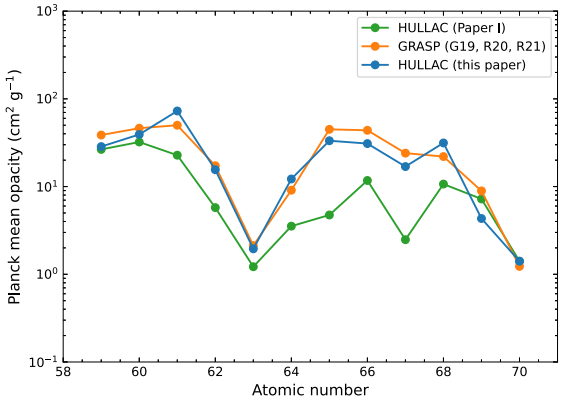

Figure 6. Plank mean opacity (for $\rho = 10^{-13}$ g cm^{-3} and $T = 5000$ K at $t = 1$ d after the merger) as a function of atomic number.

Table 3. Number transitions for each ion.

Ion	$N_{\rm total}$ [a]	$N_{\rm strong}$ [b]
Pr II	417 812	62 511
Nd II	4001 851	67 934
Pm II	21 472 279	111 540
Sm II	69 895 982	35 692
Eu II	132 942 648	2330
Gd II	158 102 969	31 961
Tb II	119 471 719	98 484
Dy II	54 784 938	49 185
Ho II	15 301 547	29 399
Er II	2432 667	30 397
Tm II	205 259	3424
Yb II	8110	274

[a]Total number calculated with HULLAC in this paper. [b]The number of transitions that satisfy $gf \exp(-E_l/kT) > 10^{-5}$ at $T = 5000$ K.

plasma. To demonstrate the impact of the improved atomic data, we show the opacity of the element mixture in this section. As a representative case, we use the abundance patterns from a trajectory of $Y_{\rm e} = 0.20$ of Wanajo et al. (2014) as in Paper I. The mass fraction of lanthanides is 11 per cent in total. Note that as our improved atomic data (as well as GRASP data) are available only for singly ionized lanthanides, we calculate the opacity by only including the atomic data of singly ionized lanthanides. Thus, the actual opacities for the element mixture would be higher than those given here.

The left panel of Fig. 10 shows the expansion opacity for singly ionized lanthanides calculated for $\rho = 10^{-13}$ g cm^{-3} and $T = 5000$ K at $t = 1$ d after the merger. As expected from the opacities of individual elements, our new opacity is higher than that in Paper I in particular at $\lambda < 5000$ Å. Overall, our new opacity shows a sound agreement with that calculated with the GRASP results. At the wavelength ($\lambda = 5000$–$10\,000$ Å), however, the HULLAC opacity is lower than the GRASP opacity by a factor of about 3. This is mainly due to the difference in the opacities of Tb II, Dy II, and Ho II (see Section 3).

A similar trend is seen in the Planck mean opacities (right panel of Fig. 10). For the temperature range at which singly ionized states are dominant, the Planck mean opacities of singly ionized lanthanides from our new calculations are $\kappa = 24.4$, 27.7, and 15.4 cm^2 g^{-1} at $T = 4000$, 4500, and 5000 K, respectively. Their values are higher than those of Paper I by a factor of 1.5–1.6. ($\kappa = 16.6$, 17.5, and 10.0 cm^2 g^{-1} at $T = 4000$, 4500, and 5000 K, respectively). The opacities from GRASP results are $\kappa = 30.1$, 38.4, and 24.6 cm^2 g^{-1} at $T = 4000$, 4500, and 5000 K, respectively. These are higher than those from our new HULLAC calculations by a factor of 1.2–1.6.

In fact, for the opacity of individual elements, there are several cases showing the larger discrepancy between our new opacity and the GRASP opacity (see Figs 4, 5, A1, and A2). However, the difference in the opacity for the element mixture is rather moderate. This is because the first few lanthanides, such as Pr ($Z = 59$), Nd ($Z = 60$), and Pm ($Z = 61$), largely contribute to the opacities of the element mixture and the agreement between two calculations is good for these elements.

With this degree of difference, the impact on the kilonova light curve is limited as singly ionized lanthanides are the dominant opacity source only around $T = 4000$–5000 K. However, it is emphasized that we perform intensive investigations only for singly ionized states. A similar level of investigation for other ionization states is necessary to fully understand the impact of the accuracy in atomic calculations to kilonova light curves. For such investigation, more benchmark calculations as well as experimental measurements are important.

5 SUMMARY

In this paper, we have performed HULLAC atomic calculations for singly ionized lanthanides with improved strategies, aiming at understanding the physics of the lanthanide opacities in kilonova ejecta and necessary accuracy of atomic data. Our results show the increased number of energy levels at low energies as compared with those in Paper I. These are mainly due to the choice of more appropriate effective potentials and inclusion of more configurations in the calculations.

As a result of lower energy level distribution, the opacities calculated with our new results are higher than those by Paper I by a factor of up to 3–10, depending on the elements and wavelength range. We also present the opacities calculated by using the results of *ab initio* GRASP calculations (G19; R20; R21). Our new opacities show sound agreements with those with GRASP calculations.

Based on our results, we identify that the structure of the opacities is controlled by arrays of transitions. At $\lambda < 6000$ Å, transitions between $4f^q$ 6s and $4f^{q-1}$ 5d 6s configurations as well as those between $4f^q$ 5d and $4f^{q-1}$ $5d^2$ configurations and $4f^{q-1}$ 5d 6s and $4f^{N-1}$ 5d 6p configurations give dominant contributions. At $\lambda > 6000$ Å, transitions between $4f^q$ 5d and $4f^q$ 6p configurations and those between $4f^{q-1}$ $5d^2$ and $4f^{q-1}$ 5d 6p give dominant contributions. It is thus important to derive accurate energy distribution for these configurations.

For a lanthanide-rich element mixture with $Y_{\rm e} = 0.20$, our results give a higher opacity than that of Paper I by a factor of about 1.5. This is moderate as compared to the difference seen in the individual elements. This is because the largest contribution comes from the first few lanthanides, for which the differences between our new calculations are moderate. To fully understand the impacts of kilonova light curves, systematic investigation as done in this paper has to be performed for other ionization states.

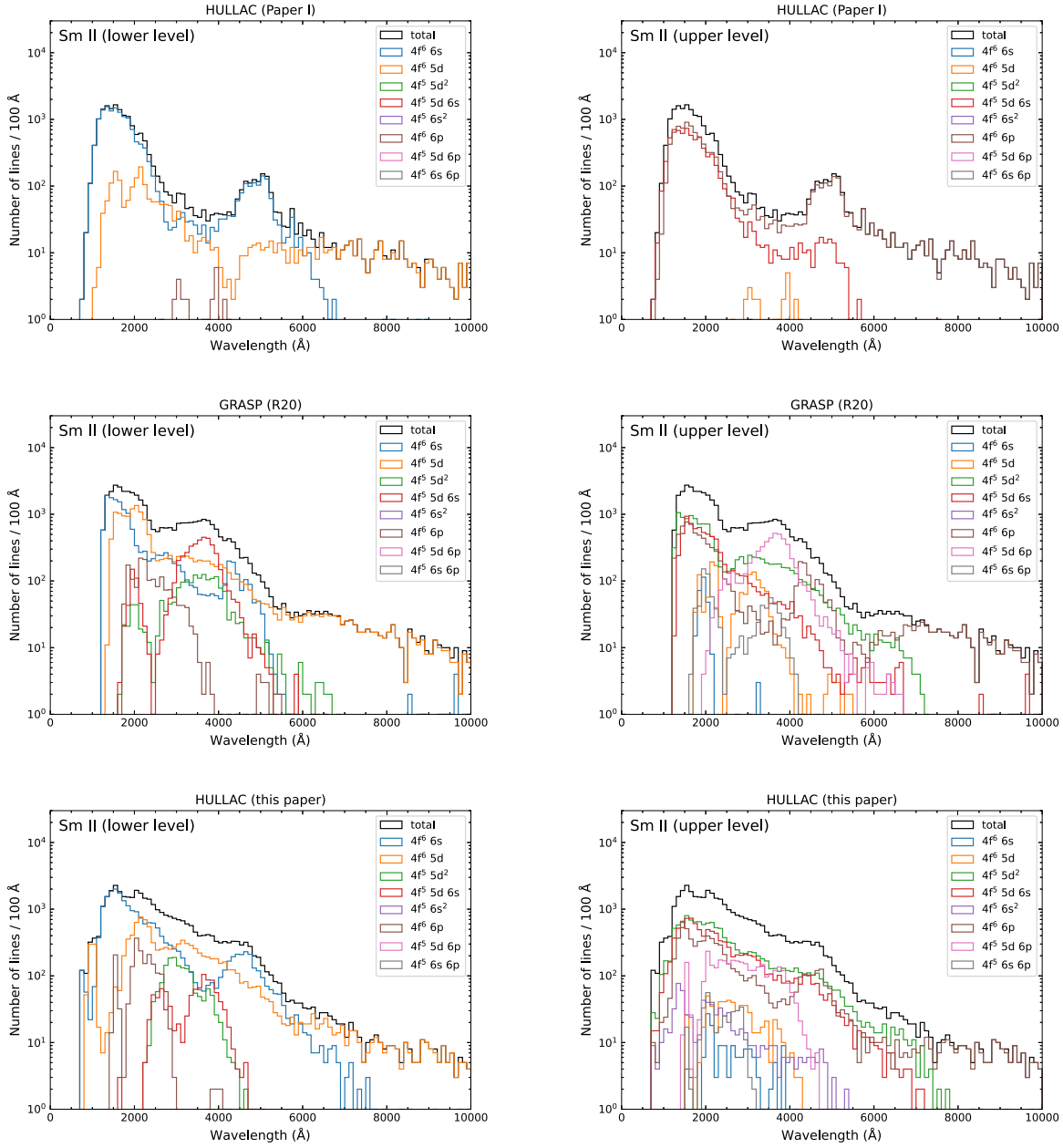

Figure 7. The number of strong lines (per 100 Å bin) for Sm II that satisfy $gf\exp(-E_l/kT) > 10^{-5}$ at $T = 5000$ K. Top, middle, and bottom panels show the cases using the HULLAC calculations in Paper I, GRASP calculations (R20), and this paper, respectively. In the left and right panels, the number of the lines is shown according to their lower and upper configurations, respectively.

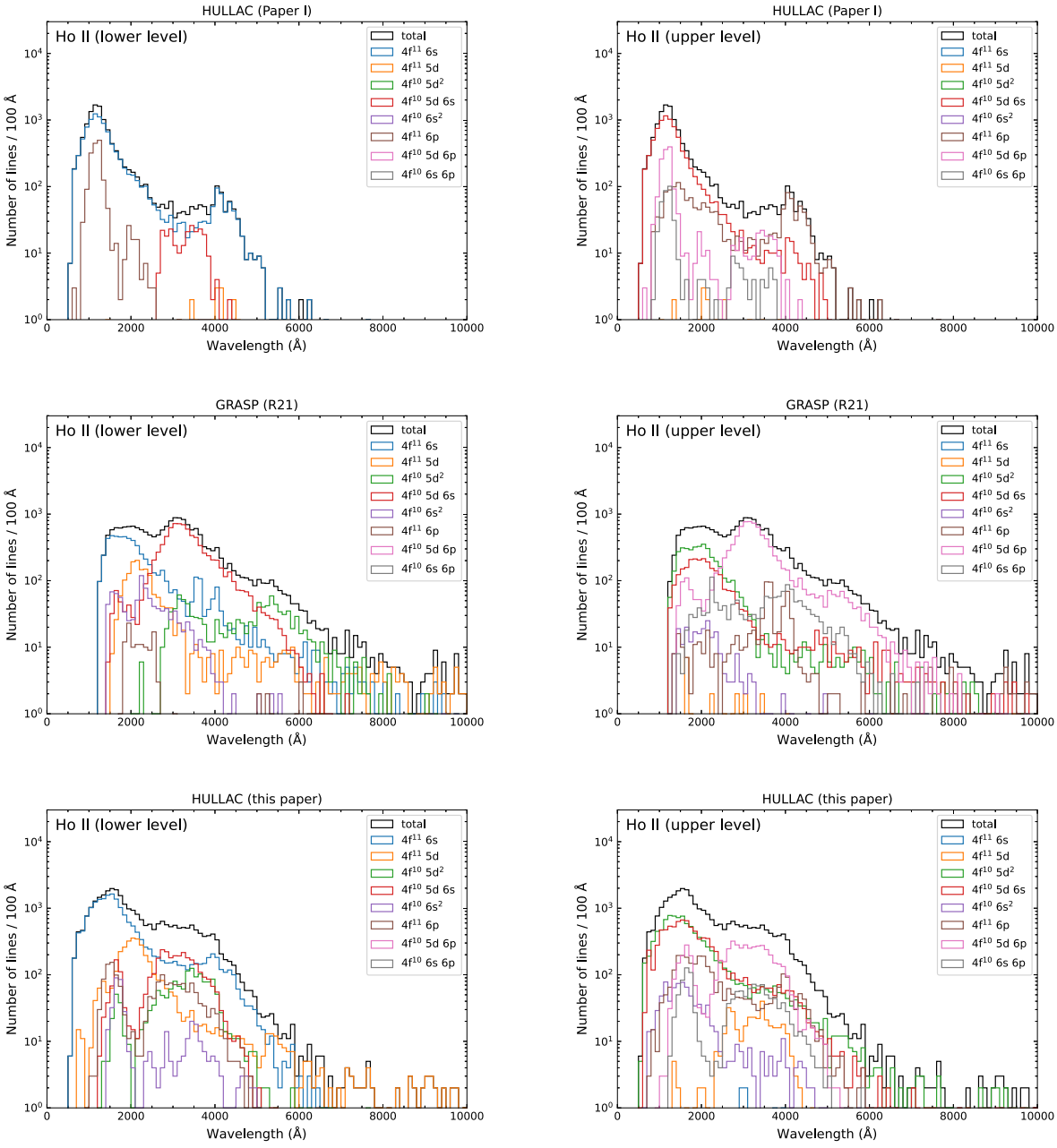

Figure 8. Same as Fig. 7, but for Ho II. GRASP results are from R21.

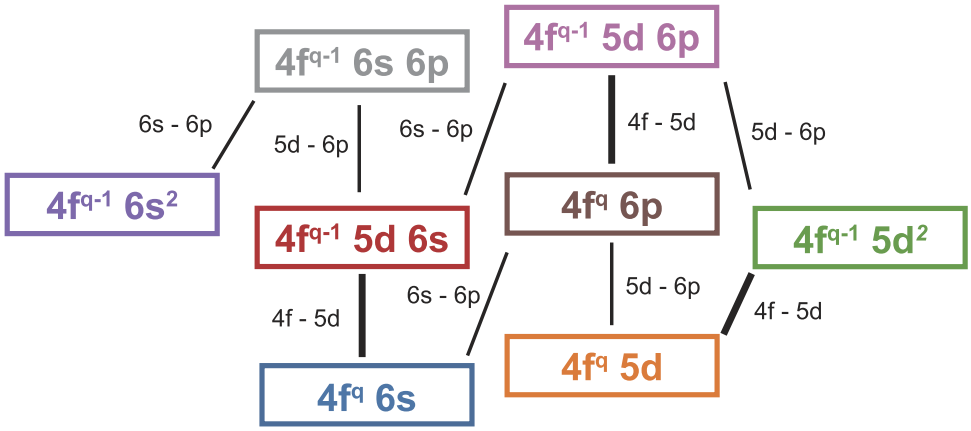

Figure 9. Schematic summary of transition arrays for singly ionized lanthanides. Colours for configurations are according to the same colour scheme in Figs 7 and 8. Since the energy levels of each configuration are widely spread, each line shows the transition in either direction depending on the energy level ordering. For Gd II, the low-lying levels of $4f^7$ 5d 6s are largely overlapping with those of $4f^8$ 6s (see Fig. 1).

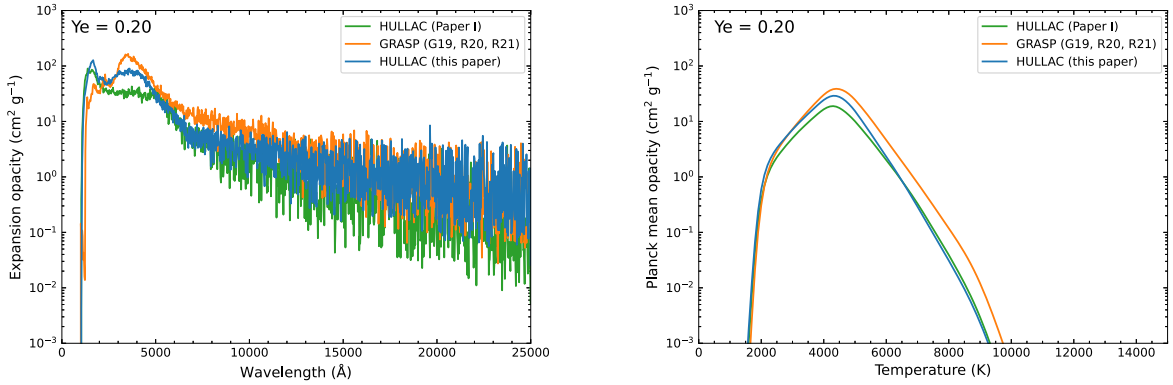

Figure 10. Opacities of singly ionized lanthanides for the element mixture with $Y_e = 0.2$. Left: Expansion opacities for $\rho = 10^{-13}$ g cm^{-3} and $T = 5000$ K at $t = 1$ d after the merger. Right: Planck mean opacities as a function of temperature. Note that the calculations include atomic data only for singly ionized ions, and actual opacities for the element mixture would be higher.

ACKNOWLEDGEMENTS

This project has received funding from the Research Council of Lithuania (LMTLT), agreement no. S-LJB-23-1, and JSPS Bilateral Joint Research Project (JPJSBP120234201).

DATA AVAILABILITY

The energy level and transition data presented in this paper are available at Japan–Lithuania Opacity Database for Kilonova: http://dpc.nifs.ac.jp/DB/Opacity-Database/.

REFERENCES

Abbott B. P. et al., 2017a, Phys. Rev. Lett., 119, 161101
Abbott B. P. et al., 2017b, ApJ, 848, L12
Banerjee S., Tanaka M., Kawaguchi K., Kato D., Gaigalas G., 2020, ApJ, 901, 29
Banerjee S., Tanaka M., Kato D., Gaigalas G., 2024, ApJ, 968, 64
Barnes J., Kasen D., 2013, ApJ, 775, 18
Bar-Shalom A., Klapisch M., Oreg J., 2001, J. Quant. Spectrosc. Radiat. Transf., 71, 169
Bauswein A., Goriely S., Janka H.-T., 2013, ApJ, 773, 78
Carvajal Gallego H., Deprince J., Berengut J. C., Palmeri P., Quinet P., 2023, MNRAS, 518, 332
Carvajal Gallego H., Pain J.-C., Godefroid M., Palmeri P., Quinet P., 2024a, J. Phys. B: At. Mol. Opt. Phys., 57, 035001
Carvajal Gallego H., Deprince J., Maison L., Palmeri P., Quinet P., 2024b, A&A, 685, A91
Eastman R. G., Pinto P. A., 1993, ApJ, 412, 731
Eichler D., Livio M., Piran T., Schramm D. N., 1989, Nature, 340, 126
Flörs A. et al., 2023, MNRAS, 524, 3083
Fontes C. J., Fryer C. L., Hungerford A. L., Wollaeger R. T., Korobkin O., 2020, MNRAS, 493, 4143
Fontes C. J., Fryer C. L., Wollaeger R. T., Mumpower M. R., Sprouse T. M., 2023, MNRAS, 519, 2862
Gaigalas G., Kato D., Rynkun P., Radžiūtė L., Tanaka M., 2019, ApJS, 240, 29 (G19)
Goriely S., Bauswein A., Janka H.-T., 2011, ApJ, 738, L32
Hotokezaka K., Tanaka M., Kato D., Gaigalas G., 2021, MNRAS, 506, 5863
Jönsson P., Gaigalas G., Bieroń J., Fischer C. F., Grant I. P., 2013, Comput. Phys. Commun., 184, 2197
Karp A. H., Lasher G., Chan K. L., Salpeter E. E., 1977, ApJ, 214, 161
Kasen D., Thomas R. C., Nugent P., 2006, ApJ, 651, 366
Kasen D., Badnell N. R., Barnes J., 2013, ApJ, 774, 25
Kasen D., Metzger B., Barnes J., Quataert E., Ramirez-Ruiz E., 2017, Nature, 551, 80

Kawaguchi K., Shibata M., Tanaka M., 2018, ApJ, 865, L21
Korobkin O., Rosswog S., Arcones A., Winteler C., 2012, MNRAS, 426, 1940
Kramida A., Ralchenko Y., Reader J., ASD NIST, 2018, NIST Atomic Spectra Database (version 5.6.1). National Institute of Standards and Technology, Gaithersburg, MD(https://physics.nist.gov/asd)
Lattimer J. M., Schramm D. N., 1974, ApJ, 192, L145
Li L.-X., Paczyński B., 1998, ApJ, 507, L59
Metzger B. D., Fernández R., 2014, MNRAS, 441, 3444
Metzger B. D. et al., 2010, MNRAS, 406, 2650
Perego A., Radice D., Bernuzzi S., 2017, ApJ, 850, L37
Pognan Q., Jerkstrand A., Grumer J., 2022, MNRAS, 513, 5174
Radžiūtė L., Gaigalas G., Kato D., Rynkun P., Tanaka M., 2020, ApJS, 248, 17 (R20)
Radžiūtė L., Gaigalas G., Kato D., Rynkun P., Tanaka M., 2021, ApJS, 257, 29 (R21)
Rosswog S., Sollerman J., Feindt U., Goobar A., Korobkin O., Wollaeger R., Fremling C., Kasliwal M. M., 2018, A&A, 615, A132
Tanaka M., Hotokezaka K., 2013, ApJ, 775, 113
Tanaka M. et al., 2017, PASJ, 69, 102
Tanaka M. et al., 2018, ApJ, 852, 109
Tanaka M., Kato D., Gaigalas G., Kawaguchi K., 2020, MNRAS, 496, 1369 (Paper I)
Wanajo S., Sekiguchi Y., Nishimura N., Kiuchi K., Kyutoku K., Shibata M., 2014, ApJ, 789, L39
Wollaeger R. T. et al., 2018, MNRAS, 478, 3298

APPENDIX A: PLANCK MEAN OPACITIES

Figs A1 and A2 show Planck mean opacities for each element. The opacities are calculated with $\rho = 10^{-13}\,\mathrm{g\,cm^{-3}}$ at $t = 1\,\mathrm{d}$ after the merger.

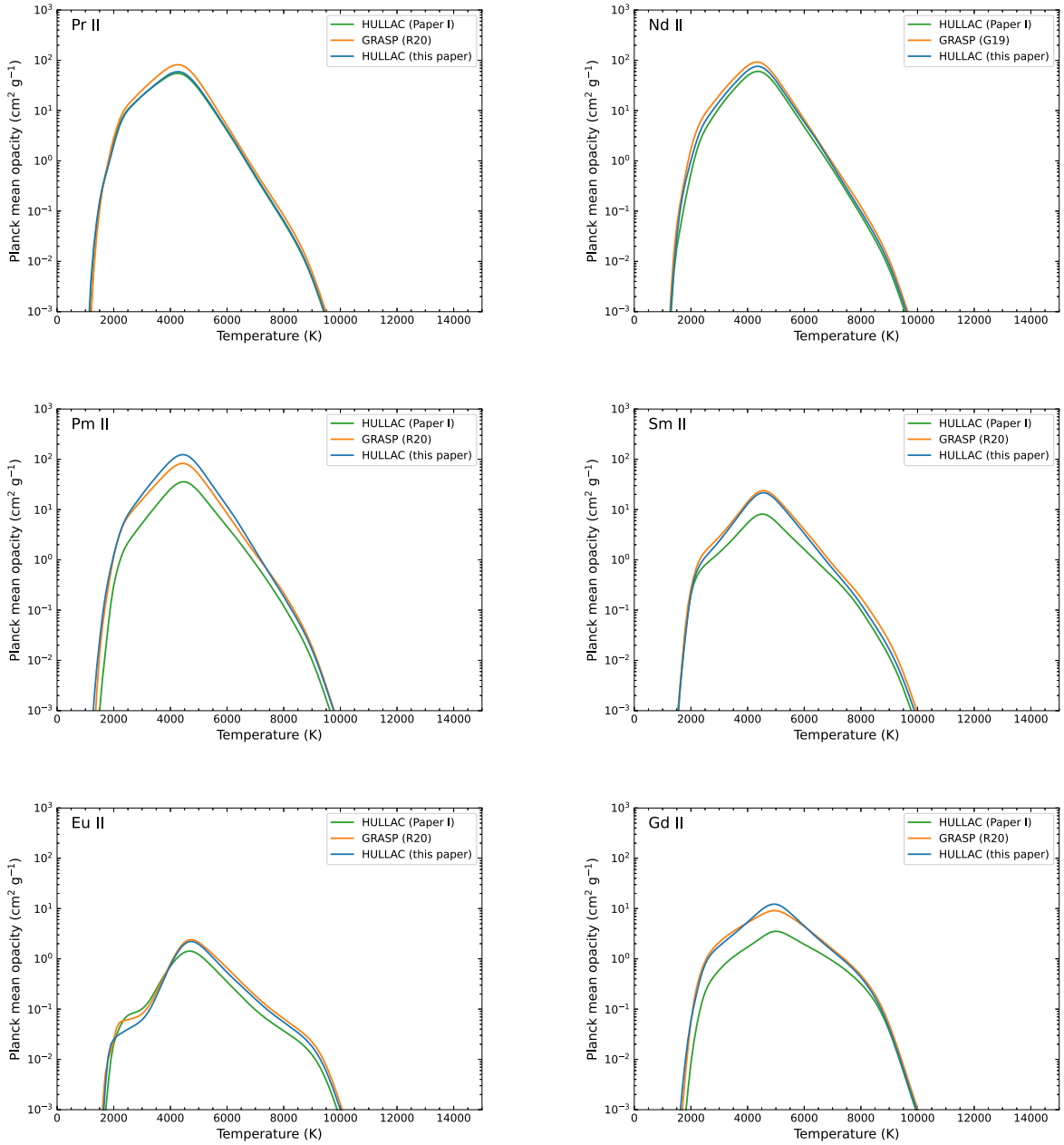

Figure A1. Planck mean opacity for singly ionized lanthanides ($Z = 59$–64) calculated from HULLAC (Paper I and this paper) and GRASP results (G19; R20; R21).

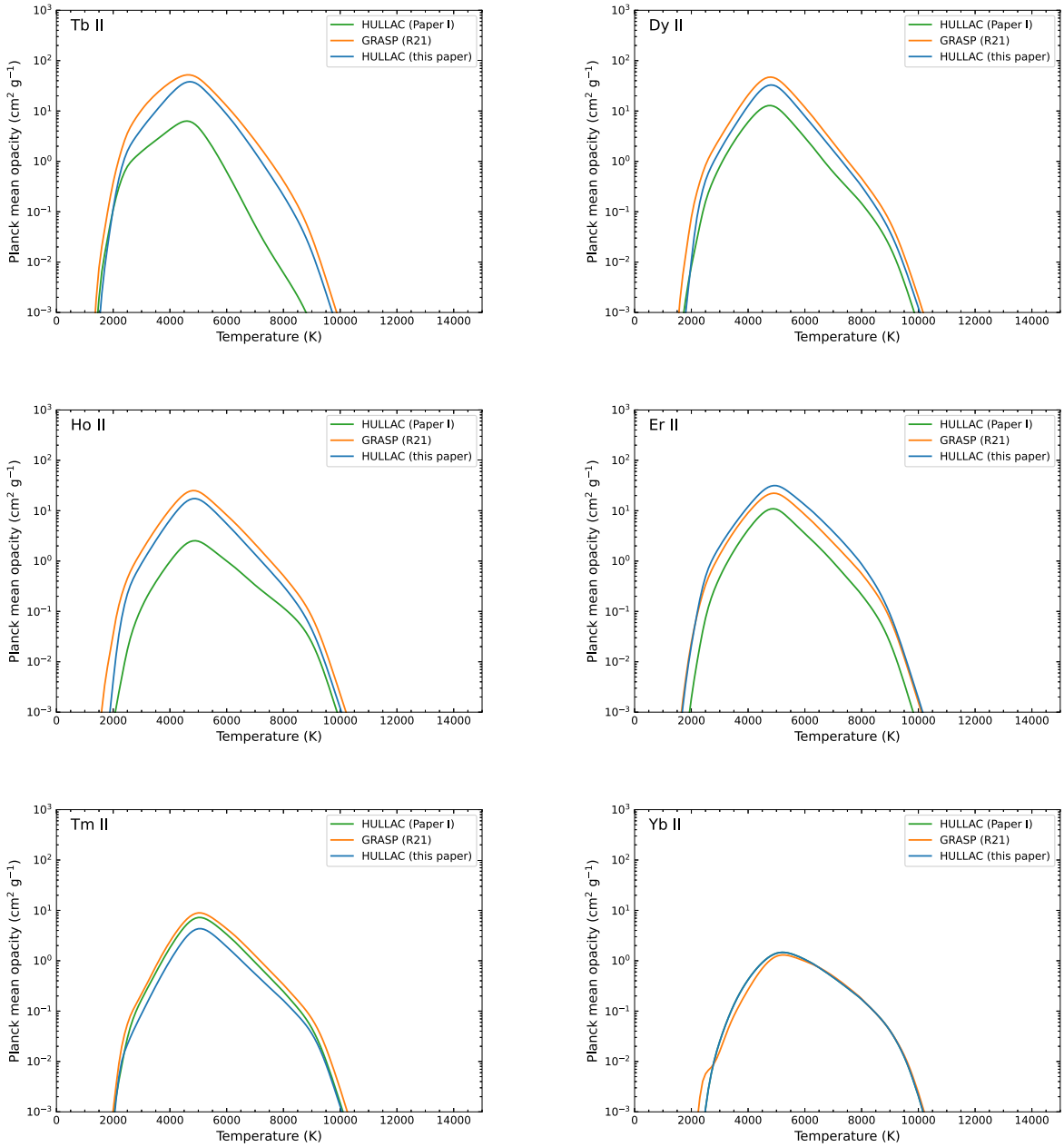

Figure A2. Same as Fig. A1, but for $Z = 65$–70. Note that the HULLAC results for Yb II in Paper I and in this paper are identical.

APPENDIX B: NATURE OF THE OPACITIES

Figs B1, B2, and B3 show the number of strong lines that satisfy $gf \exp(-E_l/kT) > 10^{-5}$ at $T = 5000$ K from our HULLAC calculations in this paper. In the left and right panels, the number of the lines is shown according to their lower and upper configurations, respectively.

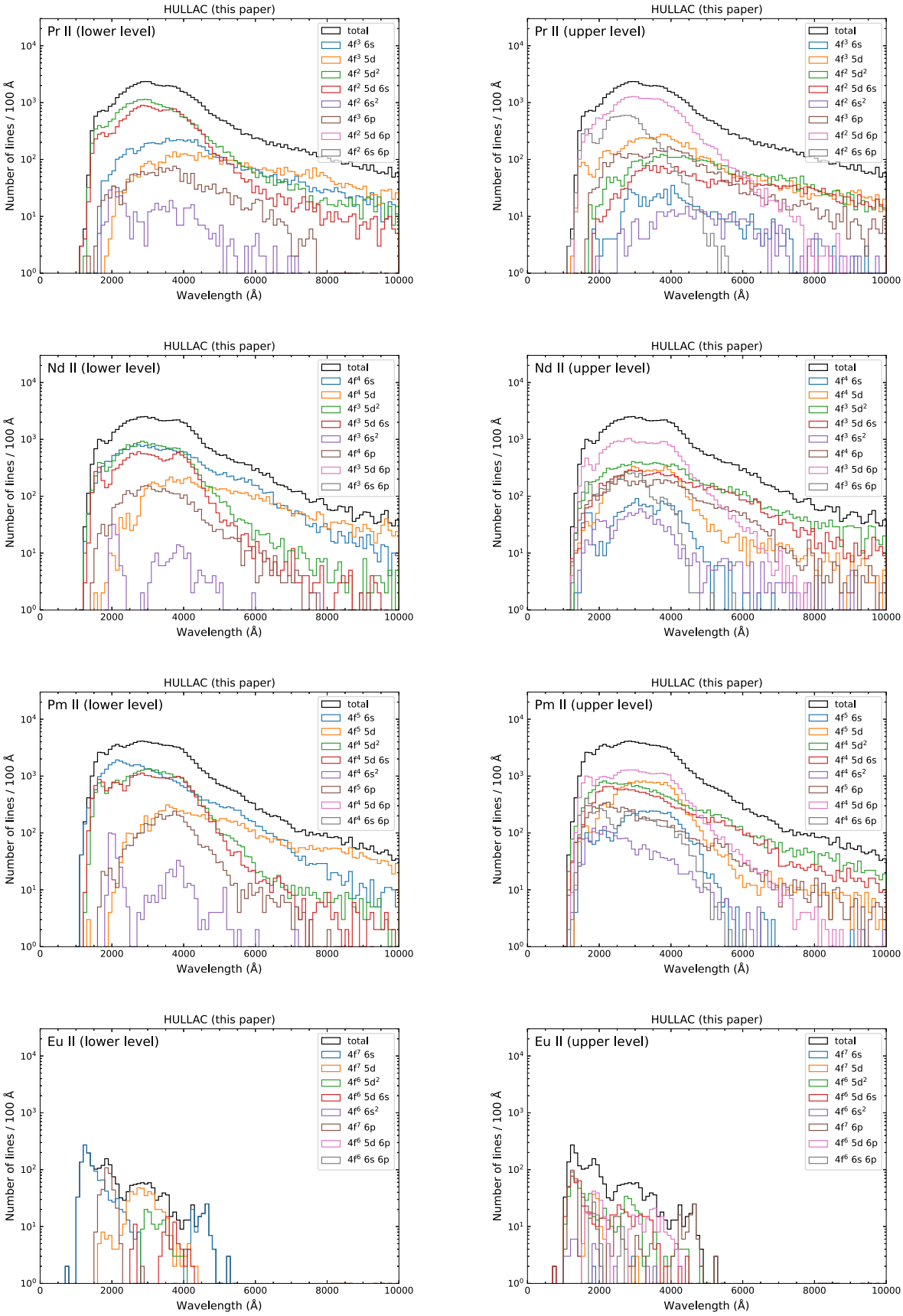

Figure B1. The number of strong lines (per 100 Å bin) for Pr II ($Z = 59$), Nd II ($Z = 60$), Pm II ($Z = 61$), and Eu II ($Z = 63$) that satisfy $gf \exp(-E_l/kT) > 10^{-5}$ at $T = 5000$ K [see Fig. 7 for Sm II ($Z = 62$)]. The results calculated with HULLAC in this paper are shown. In the left and right panels, the number of the lines is shown according to their lower and upper configurations, respectively.

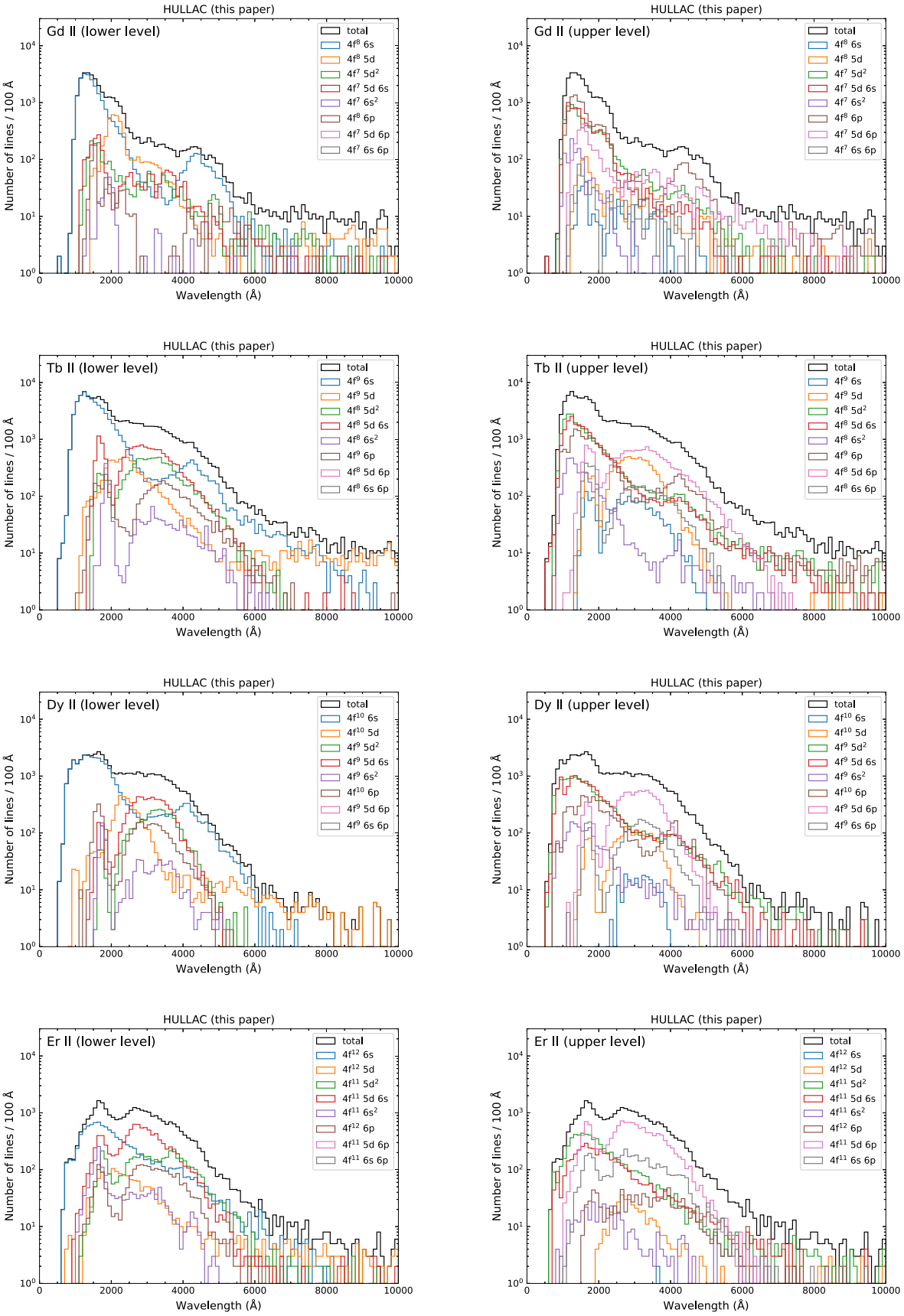

Figure B2. Same as Fig. B1, but for Gd II ($Z = 64$), Tb II ($Z = 65$), Dy II ($Z = 66$), and Er II ($Z = 68$) [see Fig. 8 for Ho II ($Z = 67$)].

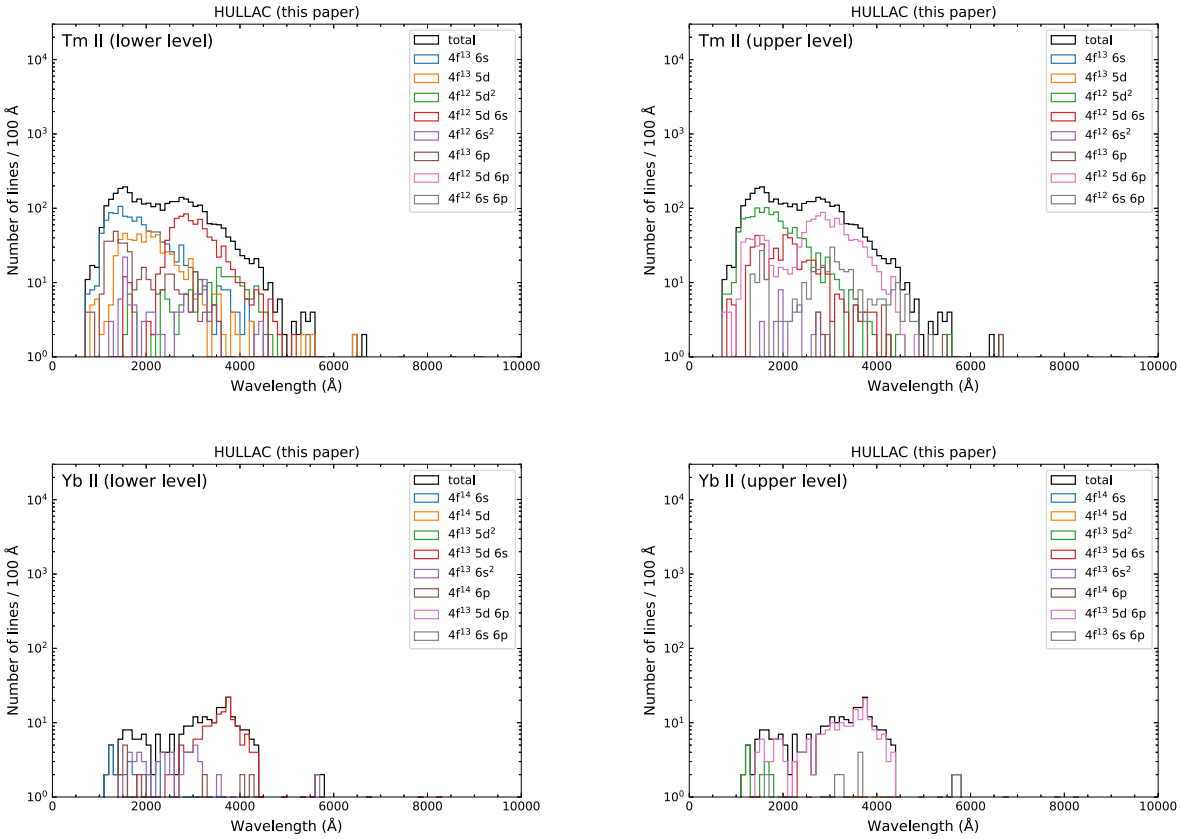

Figure B3. Same as Fig. B1, but for Tm II ($Z = 69$) and Yb II ($Z = 70$).

This paper has been typeset from a TEX/LATEX file prepared by the author.